Meas. Sci. Technol. **10** (1999) 946–955. Printed in the UK PII: S0957-0233(99)02356-5

A compact dual-crystal modulated birefringence-measurement system for microgravity applications

Jeffrey R Mackey†‡, Kamal K Das†, Shelley L Anna§‖ and Gareth H McKinley§

† NASA Glenn Research Center, 21 000 Brookpark Road, Cleveland, Ohio 44 135, USA
§ Department of Mechanical Engineering, Massachusetts Institute of Technology, Cambridge, MA 02 139, USA

E-mail: jmackey@grc.nasa.gov

Received 8 March 1999, in final form and accepted for publication 22 June 1999

Abstract. A compact modulated birefringence-measurement system has been developed for use in microgravity fluid physics applications with non-Newtonian fluids such as polymer solutions. This instrument uses a dual-crystal transverse electro-optical modulator capable of modulation frequencies in excess of 100 MHz. The two crystals are modulated 180° out of phase from each other. The theoretical framework governing the development of this instrument using the Mueller–Stokes polarization matrices is discussed. Several ground-based experiments are performed to compare this system with the theoretical results. Results from this transverse electro-optical modulator-based birefringence-measurement system agree well with the theory. The instrument is also very stable and robust, making it suitable for the extreme acceleration environment to be encountered in a NASA Black Brandt sounding rocket.

Keywords: birefringence, polarization, modulation, electro-optical, Mueller matrix, rheology

(Some figures in this article appear in black and white in the printed version.)

1. Introduction

A compact, sensitive and robust birefringence-measurement system was needed in order to perform non-invasive diagnostic tests with high sensitivity in a deforming non-Newtonian liquid bridge on an unmanned NASA sounding rocket for a microgravity research project called the 'Extensional Rheology Experiment' [1]. The entire diagnostic system was required to fit within a 15 cm long space. Commercially available instruments use modulation techniques such as the photoelastic-effect modulator (PEM) or a mechanically rotated retardation plate to produce the desired polarization-state modulation, but are too bulky for microgravity flight. Polarized light has long been used to make non-invasive measurements of many physical parameters of practical interest. Several investigators have measured Stokes vectors and Mueller matrices using Pockels cells or photoelastic modulators [2–7]. In the 1960s, Takasaki [8] developed an automatic ellipsometer using ammonium dihydrogen phosphate (ADP) cells as modulators. Ellipsometry instruments based on the use of four ADP-crystal light modulators to compensate for temperature-dependent optical bias have also been presented [9–10]. Compain and Drevillon [11] recently developed a technique based on a coupled-phase-modulator configuration using a single PEM. However, none of the available techniques is suitable for the environment that will be encountered on board a NASA Black Brandt sounding rocket, where random vibrational launching loads can reach over $15\boldsymbol{g}$ and landing shock can be in excess of $50\boldsymbol{g}$.

Since the experiment section in the rocket allowed only 15 cm of working space for the entire instrument, a PEM-based system was not practical for microgravity experiments. The experimental environment would also produce high vibrational forces that could potentially shatter the large thin quartz crystal found in a PEM or damage a mechanically rotating retardation plate. Furthermore, a single-crystal electro-optical modulator is not thermally stable [12]. For these reasons, a compact dual-crystal electro-optical modulator was chosen to perform the birefringence measurements.

In this paper, we describe a compact, robust, electro-optically modulated device capable of making independent birefringence measurements during the measurement of

‡ Present address: Analex Corporation/NASA Glenn Group, 3001 Aerospace Parkway, Cleveland, OH 44 142, USA.
‖ Present address: Harvard University, Division of Engineering and Applied Sciences, Cambridge, MA 02 139, USA.

0957-0233/99/100946+10$30.00

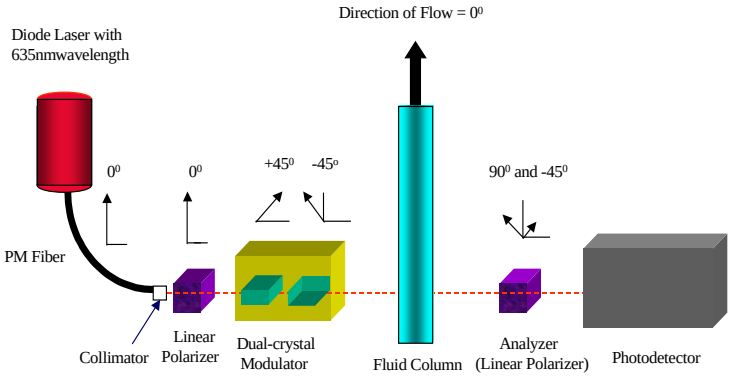

Figure 1. Optical-system elements showing polarization orientations.

the transient extensional viscosity of a polymer solution in a microgravity environment. This measurement of a microstructural variable (i.e. the chain extension and orientation) can then be coupled with macroscopic measurements of the deformation field and resulting tensile stresses in the elongating fluid sample to improve constitutive modelling of polymeric fluids [13]. The instrument design is underpinned by the Mueller-matrix calculations and its functionality is verified by ground-based experimentation. The retardance and thus the birefringence of an optically transparent anisotropic polymeric fluid can be measured accurately using this technique.

2. An overview of birefringence

Birefringence ($\Delta n'$) is defined as the anisotropy in a material's refractive index with respect to the polarization state of light propagating through it. In an optically transparent polymer material under stress, the orientation and degree of deformation of the polymer molecules cause an anisotropic polarization. If the light propagates along the z-direction through a birefringent material, the x and y components of its electrical field vector will be different from one another. This results in a phase difference or retardance (δ) as the light traverses the sample material. If the material is not dichroic, then the retardance is related directly to its birefringence. This can be expressed as [14, 15]

$$\Delta n' = n_o - n_e = -\frac{\delta\lambda}{2\pi d} \tag{1}$$

where n_o and n_e are the refractive indices for ordinary and extraordinary light rays respectively, λ is the wavelength of the light *in vacuo* and d is the sample-material thickness.

One can apply this knowledge through the use of the stress-optical law which provides a simple relationship between the material stress and the refractive-index tensor [13]. In terms of the stress components, the stress-optical law can be expressed as

$$\tau_{xy} = \frac{1}{2C}\Delta n' \sin(2\chi) \tag{2a}$$

$$\tau_{xx} - \tau_{yy} = \frac{1}{C}\Delta n' \cos(2\chi) \tag{2b}$$

where τ_{xy} is the shear stress, $\tau_{xx} - \tau_{yy}$ is the first normal stress difference, C is the material's stress-optical coefficient and χ is the instantaneous orientation angle of the molecular polymer chains with respect to the flow direction [13]. Thus, in order to unambiguously ascertain a material's state of stress, the birefringence and orientation angle must be measured simultaneously.

Figure 1 shows schematically the layout of the optical train of the birefringence instrument used to accomplish both of these objectives. The solid-state laser system is coupled to a polarization-maintaining optical fibre. A collimating lens is rigidly attached to the output end of the optical fibre. This assembly provides a collimated output beam with a spot size of less than 300 μm at the interface with the fluid column. Using a Brewster-angle window, the input polarizer is aligned in the same direction as the extensional fluid flow. Henceforth, all angles specified are referenced with respect to this flow axis (shown as vertical in figure 1). The electro-optical modulator is inserted with the two modulating crystals oriented at $\pm 45^\circ$. The analyser can be oriented at 90° (crossed polarizers) or at -45° with respect to the input polarization state. The crossed polarizer configuration is used for initial system alignment whereas the -45° configuration is used in the actual data gathering. The high-speed photodetector uses a silicon PIN diode which is polarization-insensitive so that its orientation can be arbitrary.

3. Dual-crystal transverse-electro-optical modulation technique

In order to develop a dual-crystal-modulation theory, it is helpful to present some mathematical formalism regarding the representation of polarized light and its interaction with matter. This will be done using the Stokes parameters and Mueller-matrix representations of the optical elements. It is also necessary to present the transverse electro-optical effect or Pockels effect and its application to the $LiNbO_3$ crystals used in the experimental instrument. The transverse electro-optical effect will be examined first.

A birefringent crystal possesses two distinct indices of refraction. These indices are represented by n_o and n_e which are the ordinary and extraordinary index of refraction respectively. When a voltage is applied across the crystal in a direction normal to the direction of light propagation, the difference between the polarization-sensitive refractive

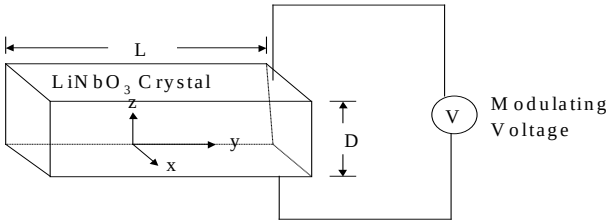

Figure 2. The transverse electro-optical crystal configuration.

indices changes. This change results in a voltage-sensitive phase retardance between the ordinary and extraordinary light rays, which can be mathematically expressed as [15]

$$\Delta\phi = \frac{2\pi}{\lambda}|n_o - n_e|L - \frac{2\pi}{\lambda}r_{33}n_o^3\frac{VL}{D} \tag{3}$$

where r_{33} is the appropriate electro-optical coefficient, L is the crystal length, D is the distance between the electrodes and V is the voltage applied across the crystal. If V is an alternating voltage, the electrical field vector or polarization state of the light passing through the crystal can be modulated. For 5 mol% MgO-doped $LiNbO_3$, $n_o = 2.2792$ and $n_e = 2.1916$ at 20 °C for light with a wavelength $\lambda = 632.8$ nm [16]. A typical transverse electro-optical crystal configuration is shown in figure 2.

In practice, the electrodes are usually made of gold deposited on the entire top and bottom surfaces of the electro-optical crystal material. The crystal material acts much the same as a capacitor would in the alternating-current electrical circuit. In the present work, a model having a very thin braided gold bonding wire to connect the electrodes with the modulator-driver circuitry was used. The $LiNbO_3$ crystals were also coated with an anti-reflective coating optimized for visible light instead of the usual near-infrared coatings used for most fibre-optical communications applications. From equation (3), the electro-optical effect is maximized when the electrical field vector of plane-polarized light is incident on the left-hand crystal face at a 45° angle with respect to the z-axis.

The Stokes vector, $\boldsymbol{S}$, consists of four parameters that characterize the polarization state of light. These parameters are denoted I, Q, U and V. They are based on the amplitude and orientation of the electrical field vector [14, 15, 17]:

$$\boldsymbol{S} = \begin{bmatrix} I \\ Q \\ U \\ V \end{bmatrix} = \begin{bmatrix} E_x^2 + E_y^2 \\ E_x^2 - E_y^2 \\ 2E_xE_y\cos(\delta) \\ 2E_xE_y\sin(\delta) \end{bmatrix}. \tag{4}$$

In equation (4), E_x and E_y are the time-dependent x and y electrical field vector components. The parameter I represents the intensity of the light while the parameters Q, U and V specify its state of polarization.

The polarization state of the output light can be modelled using the Stokes vector of the incident light multiplied by the Mueller matrices of the individual optical elements. The multiplications are performed from right to left (to match the order in which the transmitted light beam encounters each optical element) and ultimately generate the output Stokes vector which contains the required information about the anisotropy of the material under study.

For the dual-crystal instrument in our experiment, we have the polarization-state configuration shown in figure 1 with the analyser at −45°. Denoting the intrinsic static birefringence of each modulator crystal by ε, the Mueller matrices for the various optical elements are given as follows [13]. For the analyser at −45°

$$\begin{bmatrix} 1 & 0 & -1 & 0 \\ 0 & 0 & 0 & 0 \\ -1 & 0 & 1 & 0 \\ 0 & 0 & 0 & 0 \end{bmatrix}.$$

For a sample with time-variant retardance δ and time-variant orientation angle χ:

$$\begin{bmatrix} 1 & 0 & 0 \\ 0 & \cos^2(2\chi) + \sin^2(2\chi)\cos(\delta) & \sin(2\chi)\cos(2\chi)[1-\cos(\delta)] \\ 0 & \sin(2\chi)\cos(2\chi)[1-\cos(\delta)] & \sin^2(2\chi) + \cos^2(2\chi)\cos(\delta) \\ 0 & \sin(2\chi)\sin(\delta) & -\cos(2\chi)\sin(\delta) \end{bmatrix}$$
$$\begin{bmatrix} 0 & 0 \\ -\sin(2\chi)\sin(\delta) & \cos(2\chi)\sin(\delta) \\ \cos(2\chi)\sin(\delta) & \cos(\delta) \end{bmatrix}.$$

For the first $LiNbO_3$ crystal at +45° with a sinusoidal modulating electrical field applied with frequency ω:

$$\begin{bmatrix} 1 & 0 & 0 & 0 \\ 0 & \cos[A\sin(\omega t)+\varepsilon] & 0 & -\sin[A\sin(\omega t)+\varepsilon] \\ 0 & 0 & 1 & 0 \\ 0 & \sin[A\sin(\omega t)+\varepsilon] & 0 & \cos[A\sin(\omega t)+\varepsilon] \end{bmatrix}.$$

For the second $LiNbO_3$ crystal at −45° having a sinusoidal modulating electrical field applied with frequency ω 180° out of phase from that of the first crystal:

$$\begin{bmatrix} 1 & 0 & 0 & 0 \\ 0 & \cos[A\sin(\omega t)+\varepsilon] & 0 & \sin[A\sin(\omega t)+\varepsilon] \\ 0 & 0 & 1 & 0 \\ 0 & -\sin[A\sin(\omega t)+\varepsilon] & 0 & \cos[A\sin(\omega t)+\varepsilon] \end{bmatrix}.$$

For the input Stokes vector (vertical P-state):

$$\begin{bmatrix} I_0/2 \\ -I_0/2 \\ 0 \\ 0 \end{bmatrix}.$$

These Mueller matrices are multiplied in reverse order in order to calculate an equivalent system matrix which is then multiplied by the input Stokes vector. The resulting Stokes vector describes the intensity and polarization of the light emerging from the last element in the system matrix.

3.1. The matrix representation for the system in data-collection mode

The Mueller matrices and input Stokes vector are applied to determine a mathematical representation of the time-varying intensity observed at the photodetector. If a polarization-insensitive photodetector such as a silicon-PIN-diode type is used, only the polarization elements listed in section 3 need be applied. Multiplying them in reverse order and by the input Stokes vector gives us the following:

[output Stokes vector] = [analyser at -45°]
$\times$[sample][$LiNbO_3$ at -45°]
$\times$[$LiNbO_3$ at $+45^\circ$][input Stokes vector].

This matrix multiplication yields a very lengthy resultant Stokes vector. The first element of this resultant Stokes vector is the time-varying intensity, $I(t)$, which is given by [18]

$$\begin{aligned} I(t) = {} & \frac{I_0}{2} + \frac{I_0}{2}\cos[A\sin(\omega t)+\varepsilon]\sin(2\chi)\cos(2\chi) \\ & \times \cos[-A\sin(\omega t)+\varepsilon] - \frac{I_0}{2}\cos[A\sin(\omega t)+\varepsilon] \\ & \times \sin(2\chi)\cos(2\chi)\cos[-A\sin(\omega t)+\varepsilon]\cos(\delta) \\ & -\frac{I_0}{2}\cos[A\sin(\omega t)+\varepsilon]\cos(2\chi)\sin(\delta) \\ & \times \sin[-A\sin(\omega t)+\varepsilon] + \frac{I_0}{2}\sin[A\sin(\omega t)+\varepsilon] \\ & \times \sin(2\chi)\cos(2\chi)\sin[-A\sin(\omega t)+\varepsilon] \\ & -\frac{I_0}{2}\sin[A\sin(\omega t)+\varepsilon] \\ & \times \sin(2\chi)\cos(2\chi)\sin[-A\sin(\omega t)+\varepsilon]\cos(\delta) \\ & +\frac{I_0}{2}\sin[A\sin(\omega t)+\varepsilon]\cos(2\chi)\sin(\delta) \\ & \times \cos[-A\sin(\omega t)+\varepsilon]. \end{aligned} \tag{5}$$

By combining and simplifying the appropriate terms in equation (5) and using $I_{dc} = I_0/2$, the time-varying intensity reduces to the following equation:

$$\begin{aligned} I(t) = {} & I_{dc}\{1+\sin(2\chi)\cos(2\chi)\{2\cos^2[A\sin(\omega t)] \\ & -1+\{1-2\cos^2[A\sin(\omega t)]\}\cos(\delta)\} \\ & +2\sin[A\sin(\omega t)]\cos[A\sin(\omega t)]\cos(2\chi)\sin(\delta)\}. \end{aligned} \tag{6}$$

It is to be noted that $2\cos^2[A\sin(\omega t)] - 1 = \cos[2A\sin(\omega t)]$ and $2\sin[A\sin(\omega t)]\cos[A\sin(\omega t)] = \sin[2A\sin(\omega t)]$. For notational purposes, we define the following parameters:

$$M_{34} = \sin(\delta)\cos(2\chi) \tag{7}$$

$$M_{32} = [1-\cos(\delta)]\sin(2\chi)\cos(2\chi). \tag{8}$$

By substituting equations (7) and (8) into equation (6) and then using the sine and cosine expansions we obtain the following expression:

$$I(t) = I_{dc}\{1 + M_{32}\cos[A\sin(\omega t)] + M_{34}\sin[A\sin(\omega t)]\}. \tag{9}$$

Next, the Fourier–Bessel expansions are applied to give us an expression for $I(t)$ in terms of measurable quantities. The Fourier–Bessel expansions are written as follows [19]:

$$\cos[A\sin(\omega t)] = J_0(A) + 2\sum_{n=1}^{\infty} J_{2n}(A)\cos(2n\omega t) \tag{10}$$

$$\sin[A\sin(\omega t)] = 2\sum_{n=0}^{\infty} J_{2n+1}(A)\sin[(2n+1)\omega t] \tag{11}$$

where J_n is a Bessel function of the first kind, with $n = 0, 1, 2, \ldots$. Completing the expansion yields the final form of the equation to be used in measuring the time-varying intensity:

$$\begin{aligned} I(t) = {} & I_{dc}\{1 + M_{32}[J_0(A) + 2J_2(A)\cos(2\omega t) \\ & + \cdots] + M_{34}[2J_1(A)\sin(\omega t) + \cdots]\}. \end{aligned} \tag{12}$$

It is desired that the modulated birefringence system be calibrated by setting the electro-optical modulation amplitude such that $J_0(A) = 0$ since this greatly simplifies the final data analysis. Practical calibration methods are discussed in detail in section 4. With $J_0(A) = 0 (A = A_0)$, the calibrated expression then becomes

$$\begin{aligned} I(t) = {} & I_{dc}[1 + 2J_1(A_0)\sin(\omega t)M_{34} \\ & +2J_2(A_0)\cos(2\omega t)M_{32} + \cdots] \end{aligned} \tag{13}$$

which is written in terms of in-phase and in-quadrature signal components measurable by two heterodyning lock-in amplifiers. This occurs at the modulator-calibration-voltage set point, at which $J_0(A_0) = 0$. It can be shown that the first and second harmonics, I_ω and $I_{2\omega}$, are given as [13]

$$I_\omega = -2J_1(A_0)I_{dc} \tag{14}$$

$$I_{2\omega} = -2J_2(A_0)I_{dc}. \tag{15}$$

Equation (13) is equivalent to the result previously derived [13] using a single-element photoelastic modulator in place of the dual-crystal electro-optical modulator and neglecting the static birefringence intrinsic to the modulating element. One experimental constraint is that the second harmonic of the modulation frequency be low enough to be measured by a heterodyning lock-in amplifier. If this condition is satisfied, then two lock-in amplifiers can be used to simultaneously measure both the first and the second harmonic. Thus, the retardance, δ, and orientation angle, χ, can be measured simultaneously at any obtainable sampling time.

The following parameters are defined for notational purposes [13, 17]:

$$R_\omega = \frac{I_\omega\sqrt{2}}{2I_{dc}J_1(A_0)} \tag{16}$$

$$R_{2\omega} = \frac{I_{2\omega}\sqrt{2}}{2I_{dc}J_2(A_0)} \tag{17}$$

$$M = 1 - R_\omega^2 - R_{2\omega}^2. \tag{18}$$

The square root of 2 is required in equations (16) and (17) because the lock-in amplifiers output a root-mean-square voltage instead of peak-to-peak values. The parameters δ and χ are obtained from M_{34} and M_{32}. Equations (16)–(18) can be substituted into equation (13) to compute instantaneous measurements of the retardance and orientation angle [13]. These are given by equations (19) and (20) respectively:

$$\delta = \frac{\cos^{-1}(-R_{2\omega}^2 + R_\omega^2\sqrt{M})}{R_\omega^2 + R_{2\omega}^2} \tag{19}$$

$$\chi = \frac{1}{2}\cos^{-1}\left(\frac{|R_\omega|}{\sin(\delta)}\right). \tag{20}$$

The birefringence is then simply given by

$$\Delta n' = -\frac{\delta\lambda}{2\pi d}. \tag{21}$$

The birefringence is defined as a negative quantity in order to be consistent with previous sign conventions.

From this analysis, it is noted that the modulator's intrinsic static retardance is theoretically negated. With 'perfect' crystals, 'perfect' optics and 'perfect' alignment, this would certainly apply. However, since perfection is extremely difficult to achieve, the dual-crystal EOM effective retardance has been measured [18] to be between 3.85×10^{-4} and 4.00×10^{-4} radians depending on where the laser beam traverses the crystals and how well the optical alignment between the two crystals is achieved. From equation (3), the effective retardance of the dual-crystal transverse electro-optical modulator is related to the intrinsic static birefringence of each modulator crystal. In the microgravity flight system, each modulator crystal is 20 mm long.

The Mueller–Stokes-matrix calculations for this system in an arbitrary configuration have also been computed. From these matrix calculations, we can observe that setting the modulator crystals at $\pm 45^\circ$ will maximize the modulation depth and minimize the number of mathematical terms representing the time-variant intensity. It can also be observed that no modulation will occur when the modulator crystals are set to 0° and 90° since in this configuration all of the $A\sin(\omega t)$ terms disappear.

4. Instrument calibration

To aid in the analysis of dynamical measurements, it is beneficial to set $J_0(A)$ to zero. From equation (12), this occurs when $J_1(A) = 0.5191$ and $J_2(A) = 0.4317$. If we set the analyser to 90° and remove the sample, an equation for the modulated intensity containing only $J_0(A)$ and $J_2(A)$ terms is obtained. This calibration configuration is shown in figure 1 with the analyser at 90° with respect to the incident polarization state.

One method of calibration can be accomplished by placing the system in a 'data-collecting' configuration with the analyser at -45° and inserting a retarder into the sample space so that both I_ω and $I_{2\omega}$ signals are present. The optimum retardance setting for this occurs at $\pi/8$ radians since this is where the second harmonic is maximized and the first harmonic is half its maximum value. Thus, if we incrementally increase the modulator voltage, we will map out $J_1(A)$ and $J_2(A)$ in terms of lock-in-amplifier-output signals. If optical alignment has been performed correctly, the calibration curves should appear as shown in the Bessel function plot in figure 3.

The parameter A shown in figure 3 is proportional to the modulator-driving voltage. One can observe from figure 3 that $J_1(A)$ and $J_2(A)$ are near their peak values so that the sensitivity of the instrument is maximized when $J_0(A)$ is zero. Calibration must be performed in order to determine the correct set point for the modulator-driver circuitry. The experimental calibration results are examined in the next section.

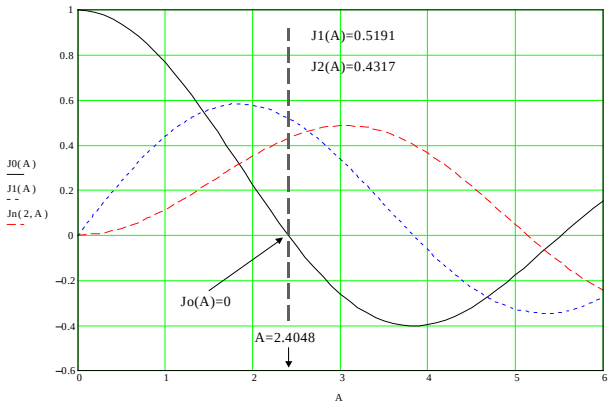

Figure 3. A modulator-calibration plot showing the desired calibration set point where $J_0(A)$ is zero.

5. Experimental testing of a microgravity flight system

In this section we compare the experimental and theoretical calibration curves generated by increasing modulator-driving voltage for the electro-optical modulator. A test using a rotating (1/16)-wave plate which has a maximum retardance of $\pi/8 \pm 0.001$ waves and a minimum retardance of zero was performed. The microgravity experimental system is shown in figure 4. The upper-left-hand image in figure 4 shows the 'optics bridge' and optical subassemblies to be used for the sounding rocket experiment. The optical assemblies include the birefringence-system detector, analyser, modulator, polarizer and (1/16)-wave-plate assembly which will be used in autophasing two heterodyning lock-in amplifiers. Also on the optics bridge are shown the digital particle-image velocimetry (DPIV) camera, lens and interference filter together with the transmitter and receiver for a laser micrometer. The image in the top-right-hand corner shows a closer view of the optical detector systems. The bottom-left-hand image shows a view of a reducing-diameter device (RDD) whose function is to give a uniform extensional shear-free flow by closing during the fluid's stretching. By closing at a predetermined rate, a cylindrical fluid column is produced at all times during the test [20]. The bottom-left-hand image also shows a DPIV camera system and light-sheet-generating optics. The bottom-right-hand image in figure 4 shows a (1/16)-wave plate attached to an armature activated by a solenoid actuator. Since the microgravity experiment will occur in an unmanned sounding rocket, all activities must be automated by computer control. The purpose of the (1/16)-wave plate is to provide first- and second-harmonic signals to the lock-in amplifiers so that autophasing can be performed. Once the lock-in amplifiers are properly autophased, the solenoid actuator moves the (1/16)-wave plate out of the birefringence system's optical path.

For ground-based testing of the birefringence system, the polarizers were crossed (the analyser was at 90°) during initial alignment in order to determine extinction ratios. The analyser was fixed at -45° when the rotating quarter-wave-plate test was conducted. The dc-photodetector-signal output was fed through a lowpass filter set to a frequency of 300 Hz. The ac-photodetector-signal outputs were sent

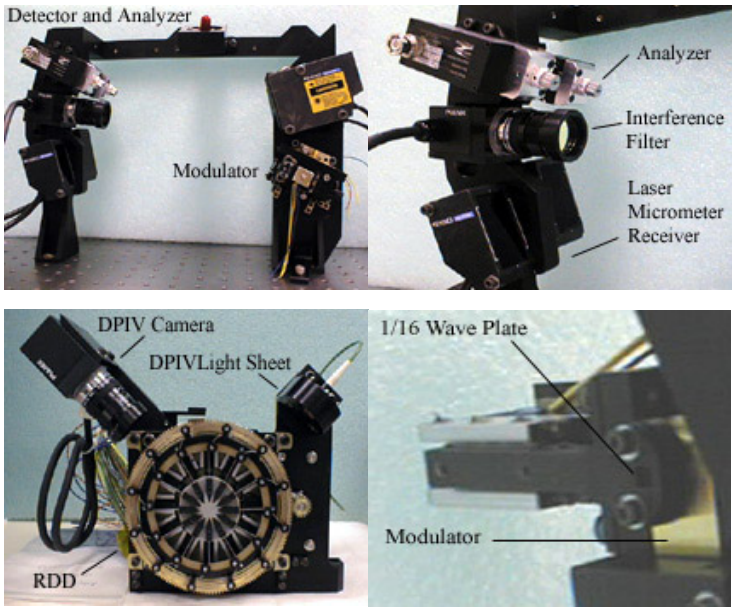

Figure 4. Experimental microgravity systems for obtaining calibration and test results.

to two heterodyning lock-in amplifiers. The modulation frequency was set to 42 kHz. This was the frequency of the first harmonic; 84 kHz was the second-harmonic frequency. The harmonic signals, I_ω and $I_{2\omega}$, were obtained from the rear analogue output panels of the first- and second-harmonic lock-in amplifiers respectively. The dc signal, I_{dc}, was obtained from the lowpass-filter output. All signals were digitized by a data-acquisition system using Labview^{TM} software.

The signal-acquisition-timing synchronization was considered carefully. Since the analysis given in equations (19)–(21) is based on signal ratios at exactly the same time, a time lag for any of the three signals will give incorrect results. Therefore, electronic-cable lengths, lock-in-amplifier time delays and other electronic-component choices must be carefully considered before proceeding.

Once the timing synchronization of the three signals had been established, the modulator calibration was performed. A resonant electro-optical modulator (New Focus, Inc, model 4103) was used so that the required driving voltages were very low. This is desired for microgravity applications where electrical power is limited. The modulation voltage was slowly incremented from 0 V RMS to 3.5 V RMS. The retardance was inferred from the modulator-driving voltage in order to compare the results with the expected values. This curve generates a scaled version of the first two Bessel functions. The experimental and theoretical calibration curves for the dual-crystal transverse electro-optical modulator are shown in figure 5.

Standard calibration methods may be performed by configuring the analyser at several different orientation angles and incrementing the modulator-driving voltage at each analyser-orientation angle [21]. Plots of the dc signal as a function of the modulator voltage for several analyser-orientation angles should intersect at a point where $J_0(A) = 0$. One problem with the standard calibration method is that it gives only a single calibration point. Another potential

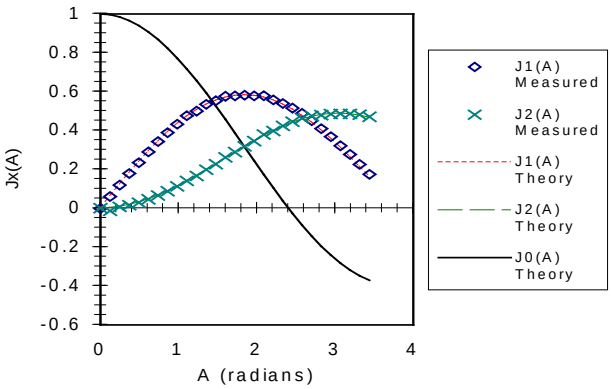

Figure 5. The Bessel-function-calibration curve for a dual-crystal transverse electro-optical modulator.

problem is that the dc signal may be subject to noise. One advantage of the new calibration method is that it performs a complete calibration sweep using both the first and the second harmonic. These signals are output from two heterodyning lock-in amplifiers, so they are much less subject to noise. Another obvious advantage is that a complete calibration curve is generated instead of a single calibration point.

5.1. Calibration-test results

In sections 5.1 and 5.2, we present the calibration-test results for the dual-crystal electro-optical modulator and for the rotating wave plate. Figure 5 shows that we obtained very good agreement between the dual-crystal-transverse-electro-optical-modulator calibration curves and the theoretical calibration curves. Figure 5 also shows $J_0(A)$ so that we may determine the null point from the plot. The calibration data show that $J_0(A) = 0$ when $A = 2.4048$ or $J_2(A) = 0.4317$.

The $J_1(A)$ calibration curves for the electro-optical modulator also agree closely with the theory derived from the Mueller–Stokes matrices [21–23]. Since this calibration

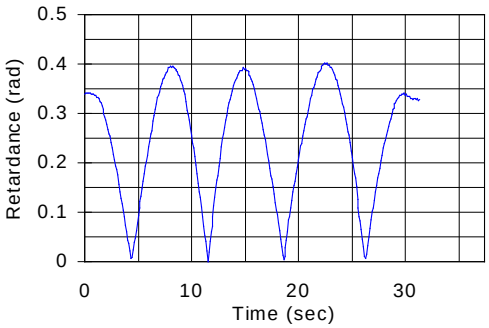

Figure 6. Retardance measurement for a rotating (1/16)-wave plate.

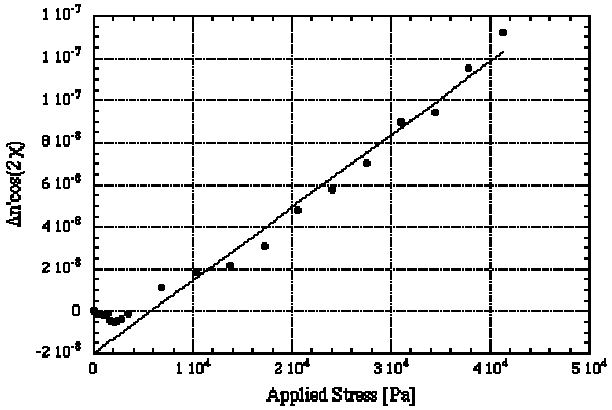

Figure 7. The birefringence as a function of the applied stress for a statically loaded PMMA rod under uniaxial tension.

requires that $J_0(A) = 0$, the second root at which $J_1(A) = 0.5191$ (after the function has gone through its maximum value) must be chosen. This is the case when the $J_1(A)$ Bessel-function curve has a negative slope. Although it is possible to perform the data analysis without setting $J_0(A)$ to zero, setting this value to zero eliminates one term from the data analysis and thus simplifies the analysis procedures.

The calibration data were used to determine a driving voltage of 1.95 V RMS for our dual-crystal transverse electro-optical modulator. This voltage was then set accordingly and the instrument was configured with the analyser at -45° as shown in figure 1.

5.2. Rotating wave-plate test results

A fused silica (1/16)-wave plate was then placed in the sample space and rotated with a constant rotational velocity. I_{dc}, I_ω and $I_{2\omega}$ signals were digitized, recorded and analysed using equations (14)–(19) to calculate δ. The data were analysed in accordance with the previously described theory in order to calculate the retardance. A plot of the retardance as a function of time is shown in figure 6. With a (1/16)-wave plate rotating with a constant velocity in the sample space, retardance levels from 0 ± 0.06 to $\pi/8$ $(0.392) \pm 0.06$ radians should be observed. If the system is properly aligned and there is little or no tilt associated with the wave plate, then the dc signal should remain fairly constant while the first- and second-harmonic signals should change with time. Both harmonic signals should have zero crossings at the same points. From figure 6, the maximum retardance measured is $\pi/8 \pm 0.06$ radians and the minimum is 0 ± 0.06 radians. The values calculated above agree well to within the tolerance of the precision wave-plate values.

5.3. Extensional-rheometry-test results

5.3.1. The modified birefringence-measurement system. The birefringence-measurement system discussed in the previous sections was developed for use in an extensional rheometry experiment which will be performed on an unmanned NASA sounding rocket. A similar birefringence-measurement system was installed on a ground-based version of the extensional rheometry experiment and used to test the operation of the system in an actual non-Newtonian fluid-flow application. The earth-based birefringence-measurement system is nearly identical to the flight system described above; the principal difference between the two systems is that the ground-based system uses two single-crystal modulators rather than one dual-crystal modulator. In this case, the first crystal is not modulated, but rather acts as a compensator to counteract the effects of static birefringence and thermal drift. In spite of this modified configuration, the Mueller matrices for this system results in a nearly identical set of equations relating the measured quantities to the retardance and the extinction angle.

The driving voltage for the earth-based birefringence system was obtained by mapping out the Bessel-function-calibration curves as described in section 5.1. The calibration curves were found to agree well with those shown in figure 5 and the optimum driving voltage was taken to be 2.85 V. In addition, the signal variation due to the presence of a (1/16)-wave plate rotating with a constant angular velocity agreed well with the data shown in figure 6. This system was observed to have an offset in the dc voltage due to a very slight misalignment of the compensator crystal. In order to compensate for this intrinsic birefringence, the dc offset was measured immediately before performing each experiment and then subtracted from the I_{dc} signal prior to computing the retardance.

5.3.2. Static-tension-test results. Before investigating results for the transient elongation of a fluid filament, it is useful to examine the response of the birefringence-measurement system in the case of a steady-state experiment. In the following experiment, the retardance of a cylindrical Plexiglas rod was measured as a function of the static tensile stress in the rod, applied by suspending varying loads from the lower end of the rod. With a constant force applied to hold the rod in tension, the stress induced along the rod can be computed. From equation (2), if the rod is loaded axially such that $\chi = 0^\circ$, then the stress-optical law says that the tensile stress is related to the birefringence of the material by [24]

$$\Delta n' \cos(2\chi) = C(\tau_{11} - \tau_{22}). \tag{22}$$

Thus, this experiment will allow us to demonstrate the validity of the stress-optical law by fitting the stress-optical coefficient to measured data and comparing these with values reported in the literature. In addition, these results will

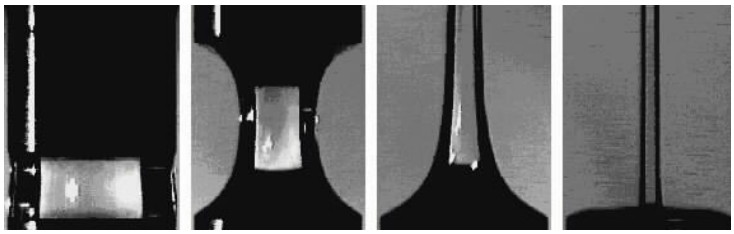

Figure 8. The diameter profile for elongation of a dilute solution of high-relative-molecular-mass polystyrene (0.025 wt%) in a styrene-oligomer resin.

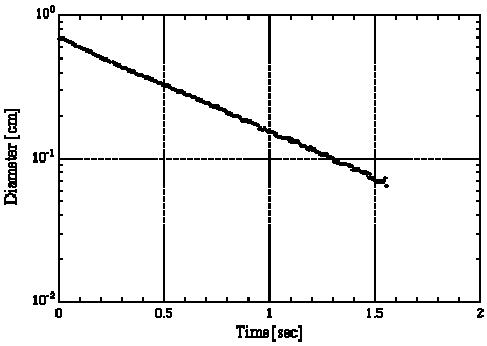

Figure 9. The fluid-column diameter as a function of time.

demonstrate the range of values measurable with the present system and will verify the reliability and accuracy of the system by using a well-understood measurement.

The tensile stress in the Plexiglas rod can be computed by performing a simple force balance on the rod. The applied force equals the weight of the applied mass and the resulting tensile stress is the ratio of this force to the cross-sectional area of the rod. By combining these equations, we find that the applied tensile stress is given by

$$\tau_{app} = \frac{4gM}{\pi D^2} \tag{23}$$

where D is the diameter of the Plexiglas rod, g is the acceleration due to gravity and M is the applied mass.

The diameter of the Plexiglas rod used in this experiment was 19.05 mm and the applied masses ranged from 1 g to 1.2 kg. For each applied mass, birefringence data were collected for several seconds after a steady-state tension had been reached, allowing average values and error bars for each measurement to be calculated.

Figure 7 is a plot of the measured birefringence as a function of the applied tensile stress for the Plexiglas-rod system described above. The birefringence is observed to increase linearly with the applied stress above a threshold value of $\Delta n' \cos(2\chi) \approx 1 \times 10^{-8}$. The slope of the linear portion of the measured curve was fitted using a least-squares fitting technique, resulting in an effective stress-optical coefficient of $C = (3.46 \pm 0.16) \times 10^{-12}$ Pa^{-1}. The quality of fit was given by $R^2 = 0.979$, which reflects an approximately 16% drift in the dc offset value over the course of the experiment.

The stress-optical coefficient of polymethylmethacrylate (PMMA), i.e. the polymeric constituent of Plexiglas, is reported in several sources. Tsvetkov [25] reports that bulk PMMA has an anisotropic polarizability in the melt that can range from -1.0×10^{-25} to $+1.8 \times 10^{-25}$ cm^3. The stress-optical coefficient is related to this quantity by [24]

$$C = \frac{2\pi(\alpha_1 - \alpha_2)(n^2+2)^2}{45kTn} \tag{24}$$

where n is the average index of refraction of the material ($n = 1.49$ for PMMA) and kT is the thermal energy. Using equation (24) to compute the stress-optical coefficient that corresponds to Tsvetkov's data, we obtain a range of $C = -4.06 \times 10^{-11}$ to $+7.5 \times 10^{-11}$ Pa^{-1}. Our measured value is well within this range and is approximately one order of magnitude lower than the maximum value reported by Tsvetkov. In addition, Niitsu *et al* [26] measured the photoelastic properties of PMMA and several glasses using a stress-analysis technique similar to the experiment described in this section. They obtained a value of $C = 0.961 \times 10^{-12}$ Pa^{-1}, which is approximately a factor of 3.6 lower than the value reported above. The apparently large discrepancy between these results could be due to some differences between the experimental methods and sample geometries used to obtain these values. Also, the PMMA samples used in each case were probably processed in significantly different ways, leading to different birefringent responses for each sample. Frattini and Fuller [27] noted that tabulated values of the stress-optical coefficient can be in error by up to 20% and thus they suggested that this quantity should be measured independently for each sample. The stress-optical coefficient value we report for the cylindrical Plexiglas rod is well within the wide range of values reported in the literature and agrees roughly with results obtained from a similar static-stress experiment.

5.3.3. Extensional rheometry. The final test we present to verify the functionality of the compact birefringence-measurement system is measurement of the transient birefringence response of a non-Newtonian fluid in an elongational flow. In a filament-stretching experiment [1, 20] such as that presented here, a fluid sample undergoes a nearly ideal elongational flow, allowing the material response of the fluid to a purely *stretching* deformation to be isolated from that due to a purely *shearing* deformation. Understanding this simple shear-free flow will help researchers to understand more complex flows, which often contain significant amounts of both stretching and shearing components. Such flows are prevalent both in industrial processes (e.g. coating and extrusion flows) and in 'benchmark' flows of academic interest (e.g. contraction flows and flow past a sphere). Since

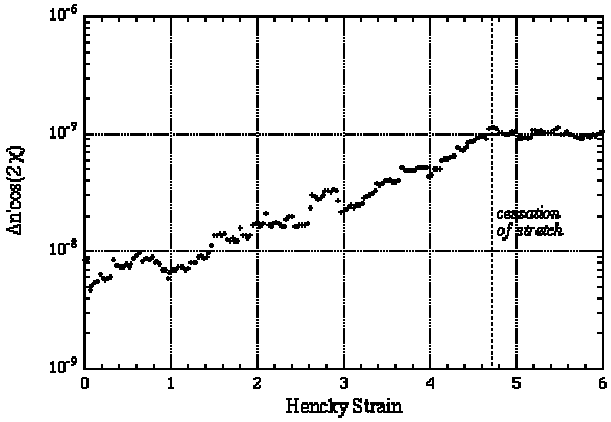

Figure 10. The measured birefringence as a function of the strain for a 0.05 wt% polystyrene solution undergoing uniaxial elongation in a filament-stretching device.

polymeric liquids exhibit surprising behaviours in many of these flows, it is desirable to understand the effect of the *microstructure* in the fluid (e.g. long polymer chains) on the *macroscopic* flow behaviour [28]. The flow-induced birefringence can be shown to be related to the molecular conformation of the polymer chains [13], so simultaneous measurements of the birefringence and the growth in tensile stress during stretching and relaxation of the fluid column will allow direct comparison of the molecular structure in the fluid with the macroscopic flow response. These simultaneous measurements will also allow an examination of the validity of the stress-optical law, which becomes increasingly invalid for strong flows in which the polymer chains are stretched near their finite extensibility limit [29].

The filament-stretching rheometer discussed in this section was presented earlier in some detailed by Anna *et al* [30] and is modelled after a similar rheometer developed by Sridhar *et al* [31]. The experiment consists of placing a small amount of fluid between two concentric circular plates. The top plate is then pulled away from the bottom plate with a velocity that increases approximately exponentially with time. The force exerted by the fluid to resist this stretching is then measured by a sensitive force transducer that is rigidly mounted onto the bottom plate. This process is illustrated by the sequence of images shown in figure 8. As the fluid column stretches and relaxes, the force data are collected together with measurements of the diameter of the column at its midpoint and measurements of the flow-induced birefringence at its midpoint. The force and diameter measurements can then be used to compute a transient tensile stress in the fluid column.

Several factors unique to the filament-stretching experiment complicate an already sensitive birefringence measurement. During the filament-stretching experiment, the midpoint diameter of the fluid column decreases exponentially with time, corresponding to the exponentially increasing length of the column. Figure 9 shows a typical diameter profile for the elongation of a dilute solution of high-relative-molecular-mass polystyrene (0.025 wt%) in an oligomeric styrene resin. The slope of this decreasing diameter is used to compute the strain rate $\dot{\varepsilon}$ of the flow

$$\dot{\varepsilon}(t) = -2\frac{\mathrm{d}\ln D_{mid}}{\mathrm{d}t}. \tag{25}$$

The Hencky strain, which is often used as a dimensionless measure of time, was obtained from the equation

$$\varepsilon(t) = -2\ln\left(\frac{D_{mid}}{D_0}\right). \tag{26}$$

The decreasing diameter of the fluid column means that the path length contributing to the total retardance of the signal is changing over at least an order of magnitude during the experiment. In addition, the surface of the fluid column is becoming increasingly curved as the diameter decreases. This radial curvature leads to undesired refraction of the laser beam such that the light impinging on the detector is fanned out and is thus becoming increasingly less intense as the experiment progresses. In addition, in a ground-based experiment, the initially unstretched fluid sample has an additional axial curvature due to gravitational sagging. As a result, the laser beam is deflected completely away from the detector surface for approximately 0.2 s at the beginning of the stretching.

Figure 10 shows a measurement of the transient flow-induced birefringence in the dilute polystyrene solution described above. The strain rate of this filament stretching experiment was $\dot{\varepsilon} = 3.0\ \mathrm{s}^{-1}$ and the final Hencky strain of the stretching portion was $\varepsilon = 4.2$. The birefringence signal increases by more than one order of magnitude during the experiment and the overall shape of the curve is consistent with measurements reported previously for a similar fluid [32]. However, even though the data were filtered using a moving-average window of order 11, large fluctuations due to noise in the system overshadowed some quantitative details of the curve shape. This large level of noise can be attributed to several factors. The most dominant contribution to the noise is evidently vibration of the motion-control system during the experiment. Baseline tests indicate that the noise levels increase by approximately one order of magnitude when the motors that move the top plate and the birefringent-measurement system are enabled and moving. This effect can be reduced by using more rigid mounts for the birefringent-measurement system that will also make alignment of the various components easier and more reliable. Other potential sources of noise and drift are electromagnetic interference and pick-up from the motor amplifiers and drift due to thermal gradients across the two single-crystal modulators. Several steps to improve the signal-to-noise ratio have been taken, including boosting the laser power to the maximum tolerable value and focusing the laser beam as another way of boosting the power delivered to the detector. Another way of reducing the noise levels, which will be investigated in the future, involves using a collecting lens to gather the fanned laser light after it has passed through the analyser [32]. Noise reduction via wavelet analysis has also been used at NASA Glenn. These noise-reduction techniques for processing of data after they have been collected are still being developed.

6. Conclusions

We have outlined the development of a dual-crystal transverse electro-optically modulated flow-induced-birefringence-measurement system that is suitable for measurement of optical anisotropy in complex fluids undergoing deformation in a microgravity environment. The choice of design configuration is based on Mueller-matrix calculations and supported by experimental calibrations. This type of modulation scheme has many advantages over existing ones. Advantages include low power consumption, low mass, small size and extreme durability. The only apparent disadvantages are the small aperture size (2 mm diameter for the unit used for the preceding tests) and the fact that $LiNbO_3$ may experience photorefractive damage at high optical power densities. Neither of these has any impact on most birefringence measurement applications. Most commercial helium–neon lasers output collimated beams with diameters of the order of 600 μm. Typical laser powers are in the range 0.5–30 mW.

Environmental testing has also been performed on many of the birefringence-system components. The modulator and laser have successfully been tested with random three-axis vibrational levels in excess of 15$\boldsymbol{g}$ while withstanding shock testing in excess of 50$\boldsymbol{g}$. The system should be capable of surviving and providing data for the five sounding-rocket test flights scheduled for the Extensional Rheology Experiment.

Acknowledgments

This work was funded as part of the NASA Glenn Research Center Microgravity Science Division's Extensional Rheology Experiment (project manager Kirk A Logsdon). GHM and SLA wish to acknowledge research support from the NASA Microgravity Science and Applications Division under award NCC3-610. In addition SLA wishes to thank the Fannie & John Hertz Foundation for fellowship support. KKD highly acknowledges the National Research Council Fellowship at the NASA Glenn Research Center.

References

[1] McKinley G H and Spiegelberg S H 1996 The extensional rheology of non-Newtonian materials *Third Annual Microgravity Fluid Physics Conf. (NASA Conf. Pub. 3338)* pp 377–82

[2] Anderson R 1992 Measurement of Muller matrices *Appl. Opt.* **31** 11–3

[3] Hunt A J and Huffman D R 1973 A new polarization-modulation light scattering instrument *Rev. Sci. Instrum.* **44** 1753–62

[4] Azzam R M A 1978 Photopolarimetric measurement of the Mueller matrix by Fourier analysis of a single detected signal *Opt. Lett.* **2** 148–50

[5] Thompson R C, Bottinger J R and Fry E S 1980 Measurement of polarized light interactions via the Mueller matrix *Appl. Opt.* **19** 1323–32

[6] Azzam R M A 1985 Arrangement of four photodetectors for measuring the state of polarization of light *Opt Lett.* **10** 309–11

[7] Iafelice V J and Bickel W S 1987 Polarized light-scattering matrix elements for select perfect and perturbed optical surfaces *Appl. Opt.* **26** 2410–15

[8] Takasaki H 1966 Automatic ellipsometer. Automatic polarimetry by means of an ADP polarization modulator III *Appl. Opt.* **5** 759–64

[9] Francois G E and Librecht F M 1972 ADP 45° x-cut four-crystal light modulator *Appl. Opt.* **11** 472–3

[10] Moritani A, Okuda Y and Nakai J 1983 Use of an ADP four-crystal electrooptic modulator in ellipsometry *Appl. Opt.* **22** 1329–36

[11] Compain E and Drevillon B 1998 High-frequency modulation of the four states of polarization of light with a single phase modulator *Rev. Sci. Instrum.* **26** 2410–15

[12] Denton R T, Chen F S and Ballman A A 1967 Lithium tantalate light modulators *J. Appl. Phys.* **38** 1611–7

[13] Fuller G G 1995 *Optical Rheometry of Complex Fluids* (New York: Oxford University Press)

[14] Azzam R M A and Bashara N M 1979 *Ellipsometry and Polarized Light* (Amsterdam: North Holland)

[15] Hecht E and Zajac A 1974 *Optics* (Melino Park, CA: Addison-Wesley)

[16] Shen H Y, Xu H, Zeng Z D, Lin W X, Wu R F and Xu G F 1992 Measurement of refractive indices and thermal refractive-index coefficients of $LiNbO_3$ crystal doped with 5 mol% MgO *Appl. Opt.* **31** 6695–7

[17] Drevillon B, Perrin J, Marbot R, Violet A and Dalby J L 1982 Fast polarization modulated ellipsometer using a microprocessor system for digital Fourier analysis *Rev. Sci. Instrum.* **53** 969–77

[18] Mackey J R 1998 Birefringence measurement system using dual-crystal transverse electro-optical modulator for microgravity fluid physics applications *Proc. Fourth Annual Microgravity and Transport Phenomena Conf.* pp 510–15

[19] Abramovitz M and Stegun J A 1965 *Handbook of Mathematical Functions* (New York: Dover)

[20] Yao M and McKinley G H 1998 Numerical simulation of extensional deformations of viscoelastic liquid bridges in filament stretching devices *J. Non-Newtonian Fluid Mech.* **74** 47–88

[21] Mackey J R, Anderson E A and Selent E 1999 Transient flow birefringent measurement system for microgravity sciences *Proc. 37th Annual AIAA Conf.* (AIAA) paper AIAA-99-0961

[22] Oakberg T 1995 Modulated interference effects: use of photoelastic modulators with lasers *Opt. Engng* **34** 1545–50

[23] Azzam R M A and Lopez A G 1989 Accurate calibration of the four-detector photopolarimeter with imperfect polarizing optical elements *J. Opt. Soc. Am.* A **6** 1513–21

[24] Fuller G G 1990 Optical rheometry *Ann. Rev. Fluid Mech.* **22** 387–417

[25] Tsvetkov V N 1964 Flow birefringence *Newer Methods of Polymer Characterization* ed B Ke (New York: Wiley) pp 563–665

[26] Niitsu Y, Ichinose K and Ikegami K 1995 Stress measurement of transparent materials by polarized laser *JSME Int. J.* A **38** 68–72

[27] Frattini P L and Fuller G G 1984 A note on phase-modulated flow birefringence: a promising rheo-optical method *J. Rheol.* **28** 61–70

[28] Bird R B, Armstrong R C and Hassager O 1987 *Dynamics of Polimeric Liquids. Volume 1: Fluid* 2nd edn (New York: Wiley)

[29] Talbot W H and Goddard J D 1979 Streaming birefringence in extensional flow of polymer solutions *Rheol. Acta* **18** 505–17

[30] Anna S L, Rogers C and McKinley G H 1999 On controlling the kinematics of a filament stretching rheometer using a real-time active control mechanism *J. Non-Newtonian Fluid Mech.* at press

[31] Sridhar T, Tirtaatmadja V, Nguyen D and Gupta R 1991 Measurement of extensional viscosity of polymer solutions *J. Non-Newtonian Fluid Mech.* **40** 271–80

[32] Spiegelberg S H, Ghosh I and McKinley G H 1999 *J. Non-Newtonian Fluid Mech.* in preparation